Check for updates

Trapping nanoscale particles *via* quasi-Scholte mode in acoustofluidics

Jiaqi Liu, [ID] [ab] Yuan Yu,[a] Rujun Zhang,[a] Yanru Chen,[b] Yanlong Guo,[a] Yi Zhang,[a] Ran Tao, [ID] [cd] Jingting Luo,[cd] Hairong Zheng,[a] Pingfa Feng,[be] Yongqing Fu, [ID] *[d] Jianjian Wang*[e] and Feiyan Cai [ID] *[a]

Non-contact and label-free acoustic manipulation of particles is crucial for various applications ranging from cell separation and tissue engineering to micromachining and nanofabrication. Surface acoustic waves (SAWs) have been widely used for microscale particle manipulation; their leaky nature in liquid often generates significant bulk acoustic streaming that undermines stable trapping of nanoscale particles. To address this challenge, we introduce an acoustofluidic device comprising a zinc oxide (ZnO) thin film deposited on aluminum foil with one-sided water loading. This design excites quasi-Scholte waves, a specialized nonleaky mode confined to the fluid–solid interface, which effectively suppresses bulk streaming and enables stable nanoparticle trapping. Both theoretical modeling and experiments confirm that the resulting strongly evanescent field operated at 5.11 MHz generates negative vertical forces and strong lateral (in-plane) trapping forces, successfully trapping 250 nm-radius particles on the foil surface. As the particle radius decreases to 150 nm, streaming-induced drag becomes the dominant manipulation mechanism. Operable at low frequencies with a simple and scalable design, our platform offers a versatile route for precise nanoscale particle trapping, with significant potential for bioengineering and nanofabrication applications.

Introduction

Acoustofluidics offers a non-contact, label-free, and highly integrated platform for manipulating suspended particles,[1–4] with broad applications ranging from cell separation[1,2] and tissue engineering[3,4] to micromachining and nanofabrication.[5–7] In this platform, particle motion is primarily governed by two distinct mechanisms, *i.e.*, acoustic radiation force (ARF) and the Stokes drag force (SDF) arising from acoustic streaming (AS). ARF is generated from momentum transfer during wave scattering and absorption with particles and enables precise single-particle manipulation. In contrast, the SDF originates from AS, which is a steady and circulatory flow generated by the nonlinear

[a] Paul C. Lauterbur Research Center for Biomedical Imaging, Shenzhen Institutes of Advanced Technology, Chinese Academy of Sciences, Shenzhen 518055, China. E-mail: fy.cai@siat.ac.cn

[b] Shenzhen International Graduate School, Tsinghua University, Shenzhen 518055, China

[c] Shenzhen Key Laboratory of Advanced Thin Films and Applications, College of Physics and Optoelectronic Engineering, Shenzhen University, Shenzhen 518060, China

[d] Faculty of Engineering and Environment, Northumbria University, Newcastle upon Tyne, NE2 2PL, UK. E-mail: richard.fu@northumbria.ac.uk

[e] Department of Mechanical Engineering, Tsinghua University, Beijing 100084, China. E-mail: wangjjthu@tsinghua.edu.cn

interaction between acoustic waves and viscous fluid absorption of acoustic energy.[8,9] Streaming may be generated in thin boundary layers along solid surfaces (*e.g.*, Rayleigh–Schlichting streaming) or in the bulk *via* acoustic energy leakage into the fluid (*e.g.*, Eckart streaming), the latter of which is especially pronounced for wave dissipation from leaky acoustic waves.[10–12]

Understanding and controlling these forces is essential for precision manipulation of particles or cells. While the ARF acts directly on individual particles, the streaming-induced SDF mobilizes particles collectively. Importantly, for Rayleigh particles (*i.e.*, particle sizes are much smaller than the wavelength), ARF scales with the particle volume, while the SDF scales with the particle radius.[13] As the particle size decreases into the nanoscale regime, ARF weakens significantly, and streaming-induced SDF may become dominant in particles' motions.[14]

Surface acoustic waves (SAWs), particularly Rayleigh waves, have been widely employed in acoustofluidic systems for particle manipulation.[15,16] As shown in Fig. 1a, Rayleigh waves are a type of nondispersive Lamb waves that propagate along the surface of the piezoelectric substrates, typically generated by interdigital transducers (IDTs) operated at frequencies in MHz and above. Their high frequency and strong surface confinement nature makes them attractive for
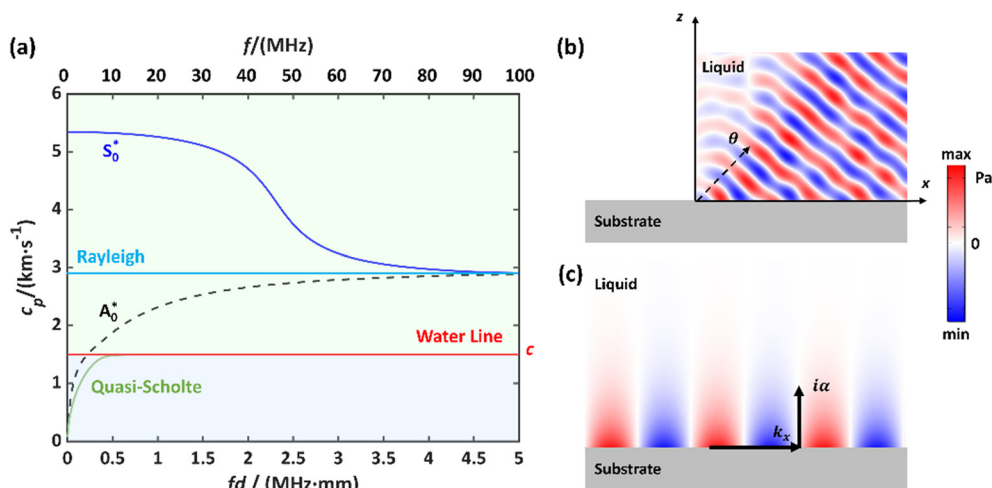
Fig. 1 Acoustic wave propagation at a fluid–solid interface. (a) The dispersion curves for the 50 μm-thick aluminum plate with one-sided water loading. Light green highlights the supersonic region, while light blue highlights the subsonic region. (b) Leaky SAW-induced pressure field in the liquid at the Rayleigh angle θ and (c) nonleaky quasi-Scholte wave-induced evanescent pressure field in the liquid. Here, k_x is the wave number in the x direction, and $k_z = i\alpha$ is the imaginary wave number in the z direction.

manipulating small particles. For example, Shi *et al.* achieved one- and two-dimensional patterning of cells and microparticles using standing SAWs (SSAWs).[17] Pan *et al.* demonstrated dynamic and reconfigurable manipulation of polystyrene (PS) particles and yeast cell clusters using SAW-based array patterns.[18]

However, when SAWs are coupled into a liquid medium as depicted in Fig. 1b, they are typically converted into leaky acoustic waves because the SAW velocity exceeds the speed of the fluid.[19] This energy leakage at the Rayleigh angle induces strong bulk AS in liquid.[20] Although this streaming phenomenon has been widely exploited for applications such as the ultrafast concentration of extracellular vesicles (EVs),[21] submicron particles,[22] and even nanoparticles,[23,24] the strong fluid disturbances caused by AS were often found to make it difficult to achieve stable trapping of nanoscale particles at MHz/GHz-range frequencies.[18,23–26]

To mitigate leaky-wave losses and reduce bulk streaming disturbances, evanescent acoustic fields have been utilized in prior studies to trap and pattern microparticles larger than 1 μm.[27–29] To extend acoustic manipulation capabilities toward nanometer scales, we explored the use of a nonleaky interfacial acoustic mode, Scholte wave, which is a type of guided wave propagating along the solid–fluid interface. It exhibits a subsonic phase velocity and a nonleaky evanescent field.[30–32] When the substrate thickness is reduced to a finite value, which has converted the substrate into a thin sheet or a plate, the Scholte wave persists but becomes dispersive, leading to what is commonly referred to as a quasi-Scholte wave (Fig. 1c).[33] Such a quasi-Scholte regime is characterized by dispersion, where the phase velocity depends on the product of frequency (f) and thickness of the plate (d).[30–32] Working within this dispersive regime for particle manipulation is advantageous. For example, a lower phase velocity results

in stronger field confinement at the fluid–plate interface, which induces stronger ARF. Aubert *et al.* experimentally demonstrated the use of a PZT-excited glass plate to generate ~2 MHz Scholte-type waves for arranging 40 μm particles and manipulating cells.[34] Our previous work also utilized this mode at 1–3 MHz frequencies for dynamic manipulation of microparticles and cells.[35–37] In prior studies, this mode was often confused and referred to as the nonleaky A_0 mode;[35–37] however, to align with recent theoretical work and standardize terminology, we refer to it as the quasi-Scholte wave in this study. In the low-frequency subsonic region, coupling occurs between the quasi-Scholte waves and the A_0^* mode (hybridized mode, which is no longer strictly antisymmetric),[38,39] but these two modes have distinctive differences. The A_0^* mode remains a pseudo-mode solid mechanical wave with a weak leakage into liquid,[33,34,40] whereas the quasi-Scholte wave is a true interface guided wave without energy leakage into the fluid,[33] contributing significantly to particle trapping by its confined acoustic field near the interface.

Although the early demonstrations validated the feasibility of quasi-Scholte wave-based trapping, their relatively low operating frequencies limited their capacity to trap nanoparticles. Because the quasi-Scholte mode exists at low values of the frequency–thickness (fd) product, achieving higher operational frequencies for nanoscale particle trapping requires a simultaneous reduction in plate thickness.[41]

In this work, we developed a zinc oxide (ZnO)/Al thin foil-based acoustofluidic platform that excites quasi-Scholte waves at relatively high frequency for achieving stable nanoscale particle trapping. Our theoretical analysis confirms that the device supports quasi-Scholte wave propagation at a frequency of around 5 MHz, producing a highly evanescent acoustic field at the fluid–Al foil

interface. This confined field generates negative vertical forces along with strong lateral (in-plane) trapping forces, enabling stable trapping of 250 nm-radius particles on the device surface. As the particle radius is decreased to 150 nm, the influence of AS becomes more pronounced, with streaming-induced drag emerging as the dominant mechanism for particle manipulation. Overall, this work introduces a new acoustofluidic strategy for nanoscale particle trapping and manipulation, offering promising potential for applications in biomedicine, microfluidics, and nanomaterials research.

Materials and methods

Device design and fabrication

To retain the frequency–thickness (fd) product within the subsonic regime while exploring higher operating frequencies, we selected thin piezoelectric foil as the substrate of the device. A thin-foil-based quasi-Scholte wave

acoustofluidic device (QSWAD) was fabricated by patterning IDTs onto a ZnO-coated aluminum foil using standard photolithography and lift-off processes. A ~4 μm ZnO film was deposited on 50 μm-thick aluminum foil via magnetron sputtering.[42] The IDTs consisted of 30 pairs of 5/50 nm thick Cr/Au interdigitated electrodes, with electrode finger widths and gaps designed to be 62.5 μm, corresponding to a wavelength of 250 μm. As shown in Fig. 2a, the two IDTs were symmetrically placed facing each other with a distance of 10 mm. The inset in Fig. 2a shows a photograph of the fabricated QSWAD. Silver paste was used to connect the wires to the pads of the IDTs.

Numerical modelling and simulation

To investigate the working mechanism of the QSWAD, COMSOL Multiphysics software (v6.1) was used for numerical modeling and simulation of physical field
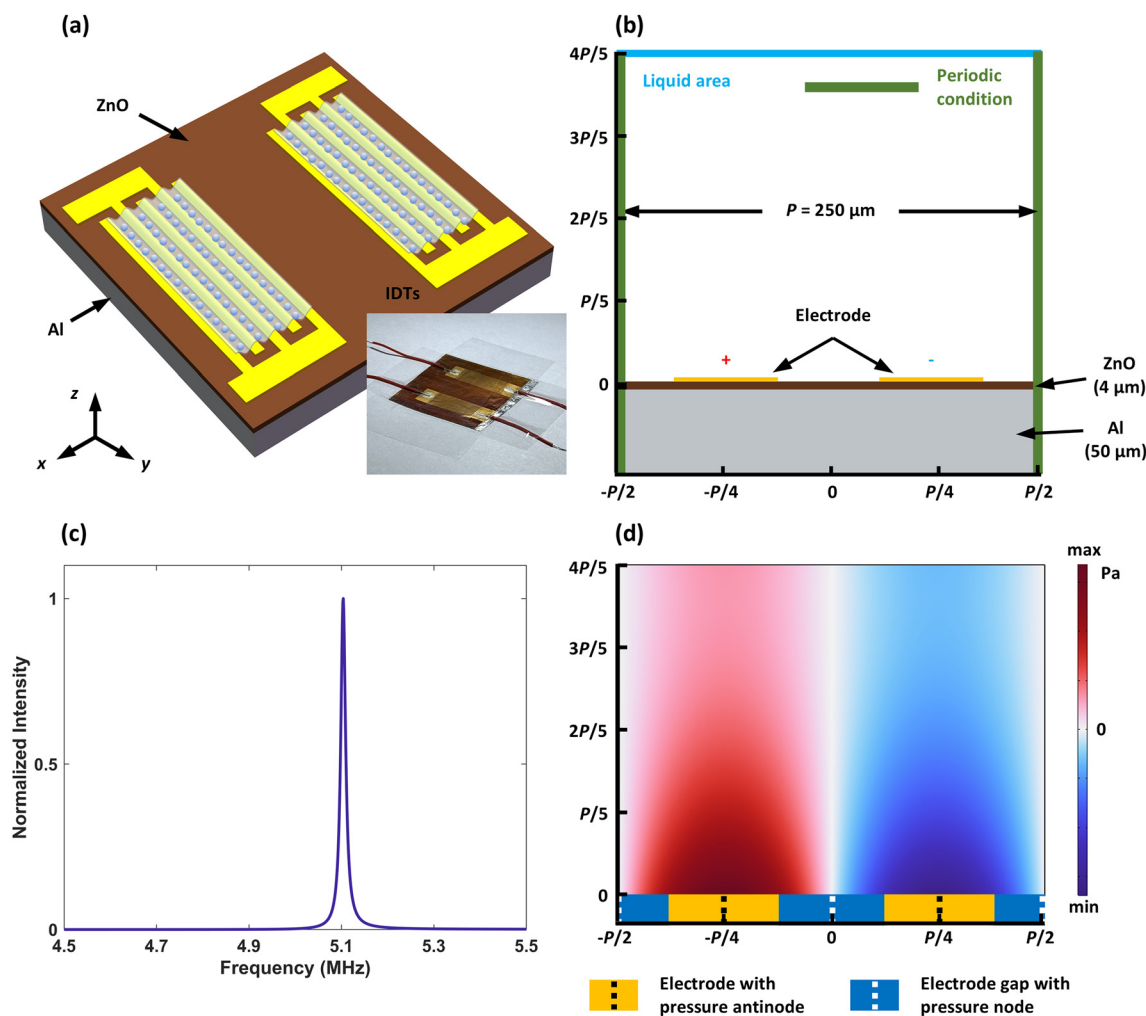

Fig. 2 Schematic diagram of the thin-foil-based quasi-Scholte wave acoustofluidic device (QSWAD) and its characteristics simulation. (a) A schematic diagram of the designed QSWAD. The inset shows a photograph of the fabricated QSWAD. (b) Schematic diagram and simulation model of one period of QSWAD side view. (c) Numerical acoustic energy intensity at the upper boundary of the liquid area. The calculated resonance frequency was 5.11 MHz. (d) The calculated resonant quasi-Scholte wave acoustic pressure field.

distribution and particle trajectories.[43,44] Fig. 2b illustrates the simulation model of the QSWAD. Given the geometrically periodic nature of the device, the numerical model was based on a single period of the IDT electrode (with a period of p = 250 μm in the x-direction). The model consisted of several components, including a 50 μm aluminum foil layer, a 4 μm ZnO layer, two electrodes positioned on the top layer of the ZnO, and a liquid medium within the working domain that was extended 200 μm above the device in the z-axis direction. In this setup, positive and negative voltages were applied to the left and right electrodes, respectively. Plane-wave radiation boundary conditions were applied to the top boundary layers, and periodic boundary conditions were applied to the left and right boundaries. To calculate the theoretical resonant frequency of the QSWAD, the acoustic energy intensity at the top boundary of the model $versus$ frequency was investigated to obtain the device's resonant spectrum.[37,45] Here, the acoustic energy intensity was calculated using the function of

$$E = \int_{\Omega} v_z \cdot p(x,z) \mathrm{d}x \tag{1}$$

where the acoustic pressure $p(x, z)$ and velocity v_z in the fluid were obtained from the COMSOL simulation.[46] The acoustic pressure field was solved using the Piezoelectric Effect Multiphysics module, and the Acoustic-Structure Boundary Coupling Multiphysics module. Additionally, the AS was solved using the AS Domain Coupling Multiphysics and Acoustic Streaming Boundary Coupling Multiphysics modules, with the dynamic viscosity of the liquid taken into account. To visualize microparticle manipulation, we simulated the motions of particles within the working domain using the Particle Tracing of the Fluid Flow module. A total of three thousand particles, with radii of 400 nm and 150 nm, were randomly released into the fluid domain, and their motions were tracked for 0–1 second using a transient study in the COMSOL simulations.

PS particle trapping experiment

In the experiment, monodispersed fluorescent PS particle suspensions (SEQ-G, Tianjin Saierqun Technology Co. Ltd, China) with a mass fraction of 1% in deionized water were used. The particle radii were 150 nm, 250 nm, and 400 nm. To facilitate observation, the above original PS particle suspension was diluted with deionized water at a ratio of 1 : 10 to prepare a new suspension for the experiment. The IDTs were applied with a voltage of 12 V and 5.396 MHz alternating current electric signals generated by a signal generator (DG4202, RIGOL, China) and then amplified by a power amplifier (LZY-22+, Mini-Circuits, USA). The prepared PS particle suspension was precisely quantified and dropped onto the IDT area using a pipette. Because the droplet is small and the device surface is non-hydrophobic,[47] the

droplet remains stably positioned at the IDT area. The trapping of particles was observed and recorded using an optical microscope (MF43-N, MSHOT, China).

Results and discussion

The excitation of nonleaky quasi-Scholte waves

The dispersion curves (*i.e.*, the phase velocity *versus* frequency) for a 50 μm-thick aluminum plate with one-sided water loading are shown in Fig. 1a. They were calculated using the open-source software Dispersion Calculator, which is based on the stiffness matrix method.[48] This figure presents an idealized case, neglecting both the presence of the piezoelectric film and the periodic electrode structure, which indicates that the quasi-Scholte mode approaches the water line as the frequency approaches ~8 MHz. Fig. S1 in the SI demonstrates a dispersion curve that considers the periodic electrode structure (with a period of 250 μm), obtained from COMSOL simulations, indicating that the quasi-Scholte mode approaches the water line when the frequency exceeds ~6.5 MHz. The difference in the cutoff frequencies may arise from variations in the numerical calculation methods used. Based on this, we designed an IDT electrode with a period of p = 250 μm on ZnO film with a thickness of ~4 μm deposited on aluminum foil. We first determined the resonant frequency and the corresponding acoustic field distribution through numerical simulations. The obtained resonant spectrum is presented in Fig. 2c, showing a distinct resonant peak at a frequency of 5.11 MHz. Fig. 2d illustrates the distribution of the acoustic pressure field in the liquid domain at this resonant frequency. The maximum pressure (or the pressure antinode) is located at the center of the electrodes (indicated by the black dashed lines), whereas the pressure is zero at the center of the electrode gap (*i.e.*, the pressure node, which is indicated by the white dashed lines). Notably, the acoustic pressure field is highly confined to the plate surface, a distinctive characteristic of the nonleaky nature of the quasi-Scholte wave. It forms a periodic field parallel to the plate and an evanescent field away from the plate surface, as shown in Fig. 2d. There is a standing wave formed at the resonant frequency ($\lambda_x = p = 2\pi/k_x$) in the x-direction, and in the z-direction, it shows a decaying acoustic wave field.[33,37]

To investigate the properties of the nonleaky quasi-Scholte waves and their effects on particle manipulations, we performed theoretical analysis of the acoustic field distribution in the liquid. The acoustic pressure of this field can be expressed as[49]

$$\phi = \phi_0 \cos(k_x x) \mathrm{e}^{-\alpha z} \mathrm{e}^{i\omega t} \tag{2}$$

where ϕ_0 is the pressure amplitude, wavenumber (m^{-1}) $k_x = 2\pi/\lambda_x$, $k_z^2 = k^2 - k_x^2 = (2\pi/\lambda_0)^2 - k_x^2$, with λ_0 being the incident wavelength. λ_x is the wavelength of the quasi-Scholte waves, which is also the period length of the electrode, *i.e.*, $\lambda_x = p$. α

is the coefficient of imaginary wavevector in the z direction k_z, and t denotes time. The α value also indicates the decay characteristics of the wave away from the surface, and can be calculated as[50]

$$k_z = i\alpha = \pm\sqrt{k^2 - k_x^2} = \pm\sqrt{\left(\frac{2\pi f}{c_0}\right)^2 - \left(\frac{2\pi}{p}\right)^2} \qquad (3)$$

where f is the resonant frequency and c_0 is the sound speed in the loading liquid. To ensure dimensional consistency, α shares the same unit as k_z (i.e., m^{-1}). A positive k_z describes an exponentially decaying evanescent wave, whereas a negative k_z implies an unphysical solution that grows exponentially with distance from the surface and is therefore generally discarded.[50] Therefore, in this paper, we inherently assume k_z to be positive, which in turn ensures that α is also positive.

The velocity field in this acoustic field can be expressed as

$$v_x = \frac{\partial\phi}{\partial x} = -\phi_0 e^{-\alpha z} e^{i\omega t} k_x \sin(k_x x) \qquad (4)$$

$$v_z = \frac{\partial\phi}{\partial z} = -\alpha\phi_0 e^{-\alpha z} e^{i\omega t} \cos(k_x x) \qquad (5)$$

The pressure can be expressed as

$$p = -\rho_0 \frac{\partial\phi}{\partial t} = -\rho_0\phi_0 \cos(k_x x) e^{-\alpha z} e^{i\omega t} \cdot i\omega \qquad (6)$$

where ρ_0 is the density of the liquid.

According to eqn (4), the acoustic field in the liquid exhibits a periodic distribution in the x-direction and an exponential decay in the z-direction. Fig. 3 illustrates the results of the distributions of acoustic pressures over a single period in the water domain under different values of α. It is worth noting that once the device materials, structure, and loading conditions are fixed, α remains constant, as the key

parameters in eqn (3), including resonant frequency f, liquid sound speed c_0, and electrode period p, do not change. Here, α_0 represents the calculated results when the substrate is a 50 μm-thick aluminum plate, and the liquid domain is deionized water (as the simulation case in Fig. 2), with a value of approximately 13172. The detailed calculation of α_0 is shown in the SI.

When $\alpha = \alpha_0$, the acoustic pressure distribution shows a localized acoustic field near the surface of the substrate, consistent with the simulation results as shown in Fig. 2d. As α is decreased or increased, the localization of the acoustic field becomes weakened (Fig. 3b) or strengthened (Fig. 3c), respectively. When $\alpha = 0$, the acoustic pressure distribution forms a one-dimensional standing wave (Fig. 3d) accompanied by energy leakage into the fluid bulk. It is confirmed that the energy of the quasi-Scholte waves in the liquid is localized near the substrate surface.

The ARF and the SDF in the AS field

Particles within the evanescent acoustic pressure field are simultaneously subjected to the combined effects of the ARF and the SDF induced by the AS in thin boundary layers. Therefore, analyzing the distributions of both ARF and AS within the acoustic field is critical to understanding how particles aggregate and move. The ARF, F^{rad}, which is the time-averaged force applied onto a particle with a radius of a in an inviscid fluid, can be estimated from the gradient of the Gor'kov potential U^{rad}:[14]

$$U^{\mathrm{rad}} = \frac{4\pi}{3} a^3 \left[\frac{f_1\kappa_0}{2}\langle p^2\rangle - \frac{3f_2\rho_0}{4}\langle v^2\rangle\right] = \frac{\pi}{2} a^3 \rho_0\phi_0^2 e^{-2\alpha z}\left[\frac{2}{3}f_1\kappa_0\rho_0\omega^2 \cos^2(k_x x) - f_2 k_x^2 \sin^2(k_x x) - f_2\alpha^2 \cos^2(k_x x)\right] \qquad (7)$$

$$\begin{aligned} F_x^{\mathrm{rad}} &= -\frac{\partial U^{\mathrm{rad}}}{\partial x} \\ &= \frac{\pi}{6} a^3 \rho_0\phi_0^2 e^{-2\alpha z} \cdot k_x \sin(2k_x x) \cdot \left[2f_1\kappa_0\rho_0\omega^2 + 3f_2 k_x^2 - 3f_2\alpha^2\right] \end{aligned} \qquad (8)$$

$$F_z^{\mathrm{rad}} = -\frac{\partial U^{\mathrm{rad}}}{\partial z} = \frac{2\pi}{3} a^3 \rho_0\phi_0^2 e^{-2\alpha z} \cdot \alpha \cdot \left[f_1\kappa_0\rho_0\omega^2 \cos^2(k_x x) - \frac{3}{2}f_2 k_x^2 \sin^2(k_x x) - \frac{3}{2}f_2\alpha^2 \cos^2(k_x x)\right] \qquad (9)$$
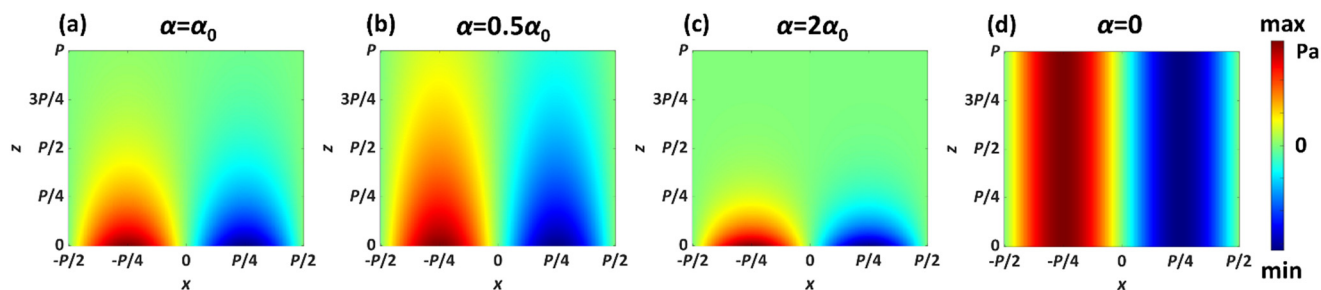

Fig. 3 The calculated pressure fields in the fluid for different values of α within one electrode period. (a–d) The pressure fields for $\alpha = \alpha_0$, $0.5\alpha_0$, $2\alpha_0$, and 0, respectively.
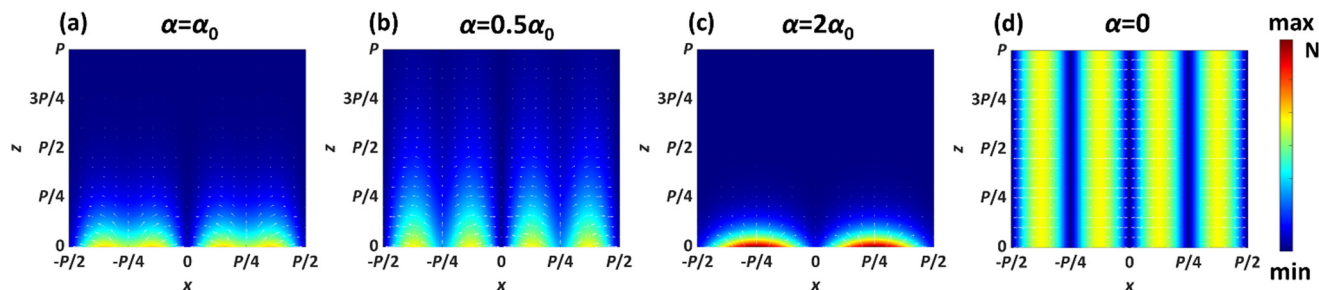
Fig. 4 The calculated ARF maps on a 400 nm-radius PS particle in the fluid for different values of α within one electrode period. (a–d) The ARF maps for $\alpha = \alpha_0$, $0.5\alpha_0$, $2\alpha_0$, and 0, respectively.

$$f_1 = 1 - \frac{\rho_0 c_0^2}{\rho_d c_d^2}, \quad f_2 = \frac{2(\rho_d - \rho_0)}{2\rho_d + \rho_0} \tag{10}$$

where f_1 and f_2 are the scattering coefficients, ρ_d and c_d are the density and the longitudinal wave velocity of the particle, respectively, c_0 is the sound speed in the fluid, and κ_0 is the compressibility of the particle. From these equations, the particles in the acoustic fields are applied with ARFs not only in the x-direction but also in the z-direction, which is perpendicular to the plate surface.

Fig. 4 illustrates the distribution of ARF on a 400 nm-radius PS particle placed over a single period in the water domain for various values of α. When $\alpha = \alpha_0$, the ARF in the z-direction F_z^{rad} exhibits negative values near the plate surface (Fig. 4a), directing the particles toward the plate. As the value of α is decreased or increased, the localization and the maximum value of the ARF are weakened (Fig. 4b) or strengthened (Fig. 4c) accordingly. When $\alpha = 0$, the vertical force F_z^{rad} remains zero, indicating no negative force in the z-direction (Fig. 4d). Combined with the results shown in Fig. 3, it is evident that the concentration of energy near the substrate surface gives rise to a negative force, which in turn traps the particles at the substrate surface.

Fig. 5a shows the variation of vertical force F_z^{rad} applied to a 400 nm-radius PS particle at the pressure node with varied α values. Here, F_z^{rad} is normalized by W/c_0, where W is the

total power.[51] When $\alpha > 0$, F_z^{rad} becomes negative near the plate surface but decays with increasing distance in the z-direction. Under the experimental conditions of this study ($\alpha = \alpha_0$), the attenuation at a half-wavelength distance reaches ~96.29%. As the α value is increased further, the maximum value of F_z^{rad} increases, but it decays quickly with increasing distance in the z-direction. When $\alpha = 0$ (*i.e.*, for 1-D bulk standing wave), F_z^{rad} becomes zero, meaning there is no negative force in the z-direction and thus no trapping effect for the particles. As a result, particles cannot be trapped on the plate surface. Fig. 5b shows the relationship between the normalized F_z^{rad} and particle size at the pressure nodes of the surface, under different values of α. It can be observed that as the particle size is increased, the absolute value of F_z^{rad} also increases. Additionally, for particles of the same diameter, a larger α results in a greater F_z^{rad}, leading to a stronger trapping effect on the particles. This indicates that for the same trapping effect, a larger α allows for the manipulation of smaller particles.

Particles also suffer from the AS-induced SDF, which can be expressed as[52]

$$F_D = 6\pi\mu a \boldsymbol{u} \tag{11}$$

where μ is the dynamic viscosity of water, a is the particle radius and $\boldsymbol{u}$ is the velocity of the surrounding flows relative
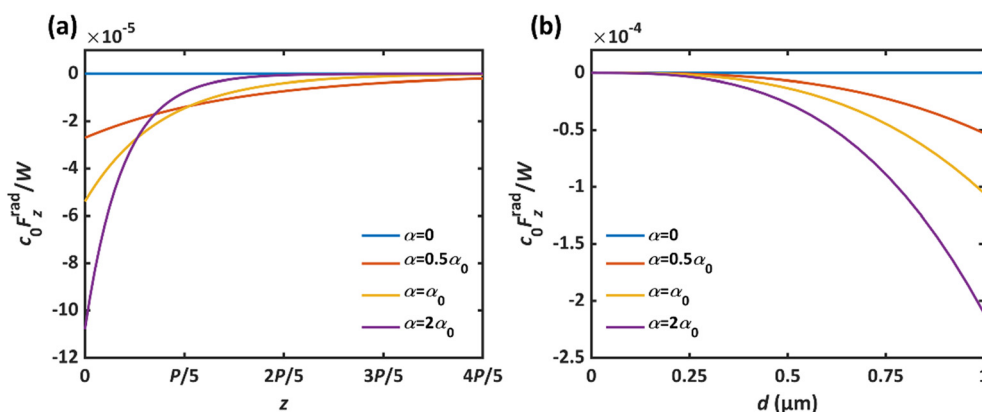

Fig. 5 Z-direction ARF at the pressure node under different values of α. (a) The variation of z-direction ARF applied to a 400 nm-radius PS particle as a function of distance from the device surface for different α values. (b) The variation of z-direction ARF at the pressure node as a function of particle diameter d for different α values.
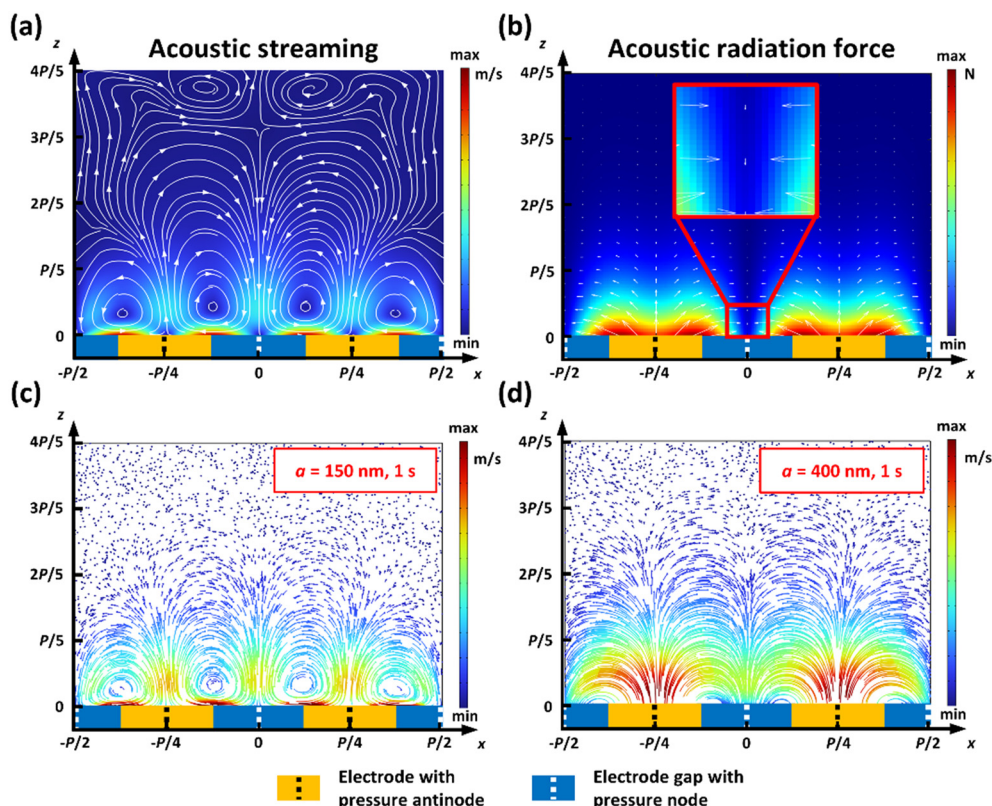
Fig. 6 Numerical simulation results of the effect of the ARF and the AS on PS particles with radii of 150 nm and 400 nm. (a) AS velocity distribution showing that the AS centers are located at the edges of the electrode fingers with arrows indicating the direction of the AS flow. (b) ARF map of 400 nm-radius PS particles, where the colour indicates the magnitude of the ARF; the length and direction of the arrows represent the magnitude and direction of the ARF. An enlarged view highlights the z-direction ARF at the pressure node. (c and d) Trajectories and final positions of PS particles with radii of 150 nm and 400 nm at time = 1 s after powering on.

to that of the particle. Fig. 6 shows the numerical simulation results of the AS velocities and the ARF distributions as well as the trajectories of 150 nm- radius and 400 nm-radius particles within the fields. Fig. 6a presents the numerical simulation results of the velocity distribution of the AS. The AS velocity peaks near the electrode edges close to the foil surface, forming four vortices per period. The streaming aligns with Rayleigh–Schlichting streaming, driven by large shear stresses within the viscous boundary layer.[11] Bulk streaming (*i.e.*, the Eckart streaming) is suppressed owing to the nonleaky mode which prevents energy dissipation into the fluid. The trajectory results of the 150 nm-radius particles, as shown in Fig. 6c, also show this feature, indicating that the 150 nm-radius particles are primarily influenced by the AS effect, which also means that the critical size (at which manipulation dominance transitions between ARF and SDF) is larger than 150 nm in radius.

Using eqn (6) and (7), the distributions of the ARFs acting on particles with a radius of 400 nm in the fluid within one period unit were calculated. The results are shown in Fig. 6b, in which the direction of the force at each point is indicated by arrows. It can be seen that the ARF is directed towards the pressure nodes. The inset of Fig. 6b shows a negative force in the z-direction at the

pressure node, which enables particles to be trapped on the plate's top surface. Fig. 6d shows the simulated trajectories of 400 nm-radius particles in the liquid within one period unit. Particles near the plate surface are aggregated at the acoustic pressure nodes without exhibiting characteristics of AS, indicating that the ARF is dominant. This also means that the critical size is smaller than 400 nm (in radius).

Our results show that particles with radii larger than 250 nm are dominated by ARF and are gathered and trapped at the acoustic pressure nodes at the center of the electrode gaps on the plate surface, achieving a parallel line pattern with its half-wavelength spacing. Particles with radii smaller than 250 nm are dominated by AS, accumulate near the electrode edges with vortex-induced rotation, forming a quarter-wavelength arrangement. Therefore, based on this design, we can trap the particles with radii down to 250 nm.

Trapping of nanoscale particles dominated by ARF

Based on the above theoretical studies of the working principle for the QSWAD, such a device can achieve precise manipulation and trapping of nanoparticles at the center of
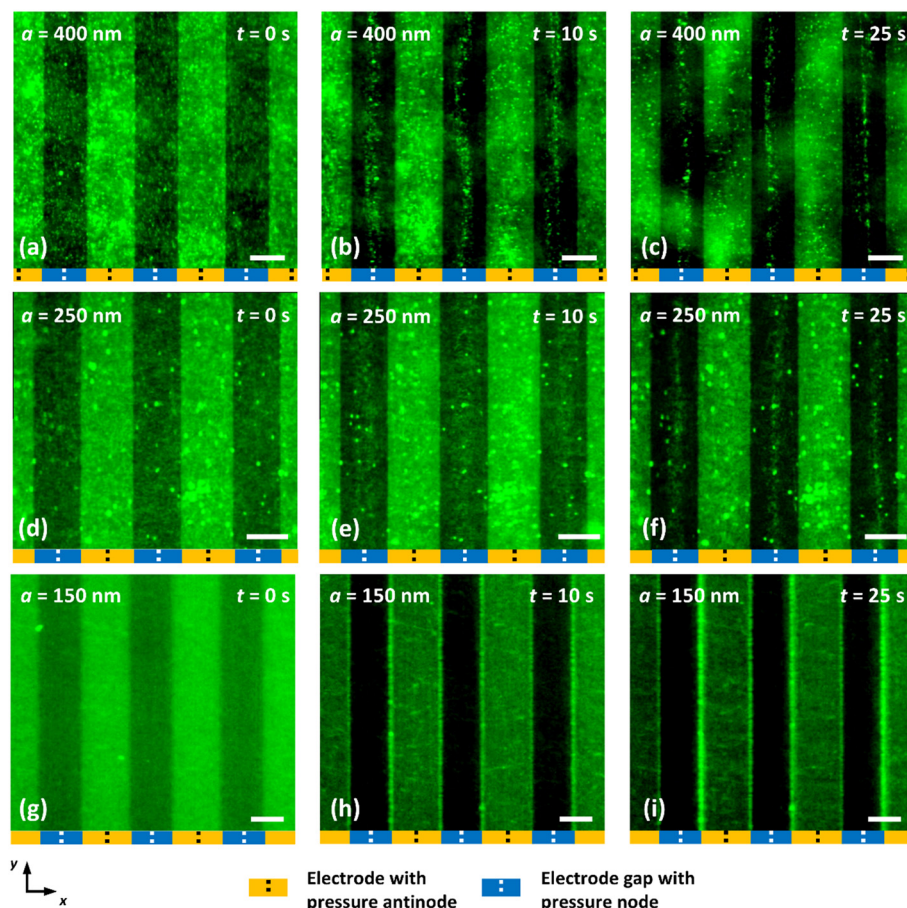
Fig. 7 Trapping and patterning of nanoscale particles in a quasi-Scholte wave field at 5.396 MHz. (a)–(c) Position of 400 nm-radius particles at 0 s, 10 s and 25 s after activation of the quasi-Scholte wave field, showing particles periodically trapped at the pressure nodes. (d)–(f) Position of 250 nm-radius particles at 0 s, 10 s and 25 s, showing particle trapping at the pressure nodes. (g)–(i) Position of 150 nm-radius particles at 0 s, 10 s and 25 s, demonstrating periodic patterning at the edges of electrode fingers. The scale bar is 50 μm.

the electrode gaps. To prove the effectiveness of the QSWAD for trapping nanoscale particles, we connected the device to a signal generator and a power amplifier and placed a drop of fluorescent suspension containing nanoscale PS particles with radii of 400 nm and 250 nm on the electrode area. After the RF power with the resonant frequency was switched on, we observed the generated patterns using an optical microscope. Fig. 7a–c show the trapping results of 400 nm-radius PS particles. Fig. 7a presents the initial distribution of particles at $t = 0$ s, where they are randomly and uniformly dispersed on the electrode surface. For the 400-nm-radius particles, upon switching on the acoustic wave power, the particles immediately began to move towards the acoustic pressure nodes between the adjacent electrodes, forming patterned parallel lines after ~10 s (as shown in Fig. 7b), and reaching a stable state after ~25 s (as shown in Fig. 7c). These particles were aligned and trapped at the acoustic pressure nodes at the center of the IDTs, forming arrays of stripes with a half-wavelength periodicity. The recorded movie for these trapping processes is shown in Video S1.

We further conducted trapping experiments with 250 nm-radius particles, with the initial and trapped states shown in Fig. 7d–f. After the acoustic wave power was switched on for ~25 s, the particles are trapped and aligned at the acoustic pressure nodes (as shown in Fig. 7f). The experimental results indicate that the QSWAD can be used to pattern particles with radii of ~250 nm at the acoustic pressure nodes. These results indicate that the particle manipulation is still dominated by the ARF in this case. It is also noteworthy that the distribution patterns of 250 nm-radius particles are significantly wider than those of 400 nm-radius particles after ~10 s of activation, indicating that the alignment speed of 250 nm-radius particles is slightly slower than that of 400 nm-radius particles. This may be because particles with a 250 nm radius are approaching the critical size based on the theoretical analysis, which has weakened the effect of the ARF. The trapping process of 250 nm-radius particles is demonstrated in Video S2.

Manipulation of nano-scale particles dominated by AS

Finally, we have conducted experiments using smaller particles. Fig. 7g–i show the patterning and manipulation results of 150 nm-radius particles. From the results of

alignment obtained after the RF power was switched on for ~10 s (as shown in Fig. 7h) and for ~25 s (as shown in Fig. 7i), the particles with radii of 150 nm are no longer dominated by ARF but rather by AS. Therefore, they become aggregated at the electrode edges, forming arrays of stripes with a quarter-wavelength periodicity, which is consistent with the simulation results as shown in Fig. 6c. The manipulation process and the trajectories of 150 nm-radius particles are shown in Videos S3 and S4. These results clearly indicate that the critical particle size for the transition between ARF and AS dominance on the QSWAD for this study lies between 150 and 250 nm (in radius).

Conclusions

In this work, we developed a ZnO/Al thin foil-based acoustofluidic platform designed for the precise and stable trapping of nanoparticles. Our theoretical analysis confirms that this device can excite nonleaky quasi-Scholte waves, generating a highly evanescent acoustic field in liquid. Theoretical and numerical analyses reveal that the evanescent acoustic field exerts both lateral ARF toward pressure nodes and vertical ARF toward the substrate. By employing a 50 μm ZnO/Al foil, we retain waves within the subsonic regime while increasing the evanescent acoustic field frequency up to ~5.5 MHz. Experiments confirm that the device can stably trap and periodically arrange particles with radii down to 250 nm. For smaller particles with 150 nm radii, manipulation becomes dominated by AS-induced SDF. Operating at a relatively low frequency, this approach provides a simple but powerful platform for stable trapping and manipulation of nanoparticles, demonstrating strong potential for applications in biomedical diagnostics, nanomaterial assembly, and microfluidic integration. Future exploration of trapping performance under dynamic flow conditions may further extend its applicability to high-throughput applications.

Author contributions

Jiaqi Liu: conceptualization, data curation, formal analysis, investigation, methodology, project administration, validation, visualization, writing – original draft, writing – review & editing. Yuan Yu: data curation, investigation, validation. Rujun Zhang: data curation, investigation. Yanru Chen: data curation, investigation, writing – review & editing. Yanlong Guo: methodology. Yi Zhang: conceptualization, resources. Ran Tao: resources. Jingting Luo: resources. Hairong Zheng: funding acquisition, resources. Pingfa Feng: funding acquisition, resources, supervision. Yongqing Fu: conceptualization, funding acquisition, resources, supervision, writing – review & editing. Jianjian Wang: conceptualization, funding acquisition, resources, supervision, writing – review & editing. Feiyan Cai: conceptualization, formal analysis, funding acquisition, methodology, project administration, resources, supervision, writing – review & editing.

Conflicts of interest

There are no conflicts to declare.

Data availability

The data that support the findings of this study are available from the corresponding author upon reasonable request. In addition, SI is available for this paper and includes the calculation of α_0, a dispersion curve that considers the periodic electrode structure, and videos showing the trapping, patterning, and trajectories of 150–400 nm particles in quasi-Scholte wave fields. See DOI: https://doi.org/10.1039/D5LC00490J.

Acknowledgements

References

1 Z. Wang, H. Wang, R. Becker, J. Rufo, S. Yang, B. E. Mace, M. Wu, J. Zou, D. T. Laskowitz and T. J. Huang, *Microsyst. Nanoeng.*, 2021, **7**, 20.

2 Y. Yang, L. Zhang, K. Jin, M. He, W. Wei, X. Chen, Q. Yang, Y. Wang, W. Pang, X. Ren and X. Duan, *Sci. Adv.*, 2022, **8**, eabn8440.

3 L. Gu, S. Jiang, X. Xu, J. Wang, F. Xu, H. Fan, J. Shang, K. Liu, U. Demirci and P. Chen, *Biofabrication*, 2023, **15**, 015019.

4 J. P. K. Armstrong, E. Pchelintseva, S. Treumuth, C. Campanella, C. Meinert, T. J. Klein, D. W. Hutmacher, B. W. Drinkwater and M. M. Stevens, *Adv. Healthcare Mater.*, 2022, **11**, 2200481.

5 C. Xu, Y. Wang, H. Pan, X. Li and D. Mei, *J. Manuf. Process.*, 2024, **112**, 179–186.

6 Y. Wang, C. Xu, J. Liu, H. Pan, Y. Li and D. Mei, *Addit. Manuf.*, 2022, **60**, 103247.

7 X. Li, K. M. Lim and W. Zhai, *Appl. Mater. Today*, 2022, **26**, 101388.

8 J. Rufo, F. Cai, J. Friend, M. Wiklund and T. J. Huang, *Nat. Rev. Methods Primers*, 2022, **2**, 30.

9 J. Friend, *Front. Acoust.*, 2023, **1**, 1261027.

10 W. Wei, Y. Wang, Z. Wang and X. Duan, *TrAC, Trends Anal. Chem.*, 2023, **160**, 116958.

11 P. B. Muller, R. Barnkob, M. J. H. Jensen and H. Bruus, *Lab Chip*, 2012, **12**, 4617.

12 S. Li, W. Cui, T. Baasch, B. Wang and Z. Gong, *Phys. Rev. Fluids*, 2024, **9**, 084201.

13 R. Barnkob, P. Augustsson, T. Laurell and H. Bruus, *Phys. Rev. E:Stat., Nonlinear, Soft Matter Phys.*, 2012, **86**, 056307.

14 M. Settnes and H. Bruus, *Phys. Rev. E:Stat., Nonlinear, Soft Matter Phys.*, 2012, **85**, 016327.

15 M. X. Lim, B. VanSaders and H. M. Jaeger, *Rep. Prog. Phys.*, 2024, **87**, 064601.

16 W. Li, Z. Yao, T. Ma, Z. Ye, K. He, L. Wang, H. Wang, Y. Fu and X. Xu, *Adv. Colloid Interface Sci.*, 2024, **332**, 103276.

17 J. Shi, D. Ahmed, X. Mao, S.-C. S. Lin, A. Lawit and T. J. Huang, *Lab Chip*, 2009, **9**, 2890.

18 H. Pan, D. Mei, C. Xu, S. Han and Y. Wang, *Lab Chip*, 2023, **23**, 215–228.

19 G. Shakya, T. Yang, Y. Gao, A. K. Fajrial, B. Li, M. Ruzzene, M. A. Borden and X. Ding, *Nat. Commun.*, 2022, **13**, 987.

20 J.-C. Hsu and C.-Y. Chang, *Micromachines*, 2022, **13**, 2175.

21 J. Rufo, P. Zhang, Z. Wang, Y. Gu, K. Yang, J. Rich, C. Chen, R. Zhong, K. Jin, Y. He, J. Xia, K. Li, J. Wu, Y. Ouyang, Y. Sadovsky, L. P. Lee and T. J. Huang, *Microsyst. Nanoeng.*, 2024, **10**, 23.

22 D. J. Collins, Z. Ma and Y. Ai, *Anal. Chem.*, 2016, **88**, 5513–5522.

23 W. Cui, L. Mu, X. Duan, W. Pang and M. A. Reed, *Nanoscale*, 2019, **11**, 14625–14634.

24 Z. Mao, P. Li, M. Wu, H. Bachman, N. Mesyngier, X. Guo, S. Liu, F. Costanzo and T. J. Huang, *ACS Nano*, 2017, **11**, 603–612.

25 J. Shi, C. Zhang, P. Li, B. Peng, X. Li, X. Liu and W. Zhou, *Appl. Phys. Lett.*, 2024, **124**, 202201.

26 Y. Hu, Y. Wang, M. Zhang, C. Gao, P. Zhao, S. Zhang, Z. Zan, D. Li and Z. Fan, *Small Sci.*, 2024, **4**, 2300146.

27 F. Li, Y. Xiao, J. Lei, X. Xia, W. Zhou, L. Meng, L. Niu, J. Wu, J. Li, F. Cai and H. Zheng, *Appl. Phys. Lett.*, 2018, **113**, 173503.

28 P.-Y. Gires and C. Poulain, *Commun. Phys.*, 2019, **2**, 94.

29 S. Surappa, S. Pavagada, F. Soto, D. Akin, C. Wei, F. L. Degertekin and U. Demirci, *Nat. Commun.*, 2025, **16**, 494.

30 M. De Billy and G. Quentin, *J. Appl. Phys.*, 1983, **54**, 4314–4322.

31 F. B. Cegla, P. Cawley and M. J. S. Lowe, *J. Acoust. Soc. Am.*, 2005, **117**, 1098–1107.

32 X. Hu, C. T. Ng and A. Kotousov, *NDT&E Int*, 2021, **117**, 102379.

33 F. Cai, J. Liu, K. Deng, Z. He, R. Zhang, Y. Li, J. Wang and H. Zheng, *J. Acoust. Soc. Am.*, 2025, **158**, 164–172.

34 V. Aubert, R. Wunenburger, T. Valier-Brasier, D. Rabaud, J.-P. Kleman and C. Poulain, *Lab Chip*, 2016, **16**, 2532–2539.

35 F. Cai, Z. He, Z. Liu, L. Meng, X. Cheng and H. Zheng, *Appl. Phys. Lett.*, 2011, **99**, 253505.

36 F. Li, F. Cai, Z. Liu, L. Meng, M. Qian, C. Wang, Q. Cheng, M. Qian, X. Liu, J. Wu, J. Li and H. Zheng, *Phys. Rev. Appl.*, 2014, **1**, 051001.

37 F. Li, F. Cai, L. Zhang, Z. Liu, F. Li, L. Meng, J. Wu, J. Li, X. Zhang and H. Zheng, *Phys. Rev. Appl.*, 2020, **13**, 044077.

38 H. Dabirikhah and C. W. Turner, *J. Acoust. Soc. Am.*, 1996, **100**, 3442–3445.

39 D. A. Kiefer, M. Ponschab, S. J. Rupitsch and M. Mayle, *J. Acoust. Soc. Am.*, 2019, **145**, 3341–3350.

40 H. Gravenkamp, B. Plestenjak, D. A. Kiefer and E. Jarlebring, *J. Sound Vib.*, 2025, **596**, 118716.

41 J.-C. Hsu and C.-L. Chao, *Appl. Phys. Lett.*, 2021, **119**, 103504.

42 R. Tao, W. B. Wang, J. T. Luo, S. Ahmad Hasan, H. Torun, P. Canyelles-Pericas, J. Zhou, W. P. Xuan, M. D. Cooke, D. Gibson, Q. Wu, W. P. Ng, J. K. Luo and Y. Q. Fu, *Surf. Coat. Technol.*, 2019, **357**, 587–594.

43 F. Cai, L. Meng, C. Jiang, Y. Pan and H. Zheng, *J. Acoust. Soc. Am.*, 2010, **128**, 1617–1622.

44 L. Meng, F. Cai, F. Li, W. Zhou, L. Niu and H. Zheng, *J. Phys. D: Appl. Phys.*, 2019, **52**, 273001.

45 Z. He, H. Jia, C. Qiu, S. Peng, X. Mei, F. Cai, P. Peng, M. Ke and Z. Liu, *Phys. Rev. Lett.*, 2010, **105**, 074301.

46 R. P. Moiseyenko and H. Bruus, *Phys. Rev. Appl.*, 2019, **11**, 014014.

47 R. Tao, G. McHale, J. Reboud, J. M. Cooper, H. Torun, J. Luo, J. Luo, X. Yang, J. Zhou, P. Canyelles-Pericas, Q. Wu and Y. Fu, *Nano Lett.*, 2020, **20**, 3263–3270.

48 A. M. A. Huber, *J. Acoust. Soc. Am.*, 2023, **154**, 1073–1094.

49 M. Settnes and H. Bruus, *Phys. Rev. E:Stat., Nonlinear, Soft Matter Phys.*, 2012, **85**, 016327.

50 E. M. Viggen and H. K. Arnestad, *J. Sound Vib.*, 2023, **560**, 117787.

51 O. A. Sapozhnikov and M. R. Bailey, *J. Acoust. Soc. Am.*, 2013, **133**, 661–676.

52 Y. Liu, Q. Yin, Y. Luo, Z. Huang, Q. Cheng, W. Zhang, B. Zhou, Y. Zhou and Z. Ma, *Ultrason. Sonochem.*, 2023, **96**, 106441.